

Joint Sparsity in SAR Tomography for Urban Mapping

Xiao Xiang Zhu, *Senior Member, IEEE*, Nan Ge, and Muhammad Shahzad, *Student Member, IEEE*

Abstract—With meter-resolution images delivered by modern synthetic aperture radar (SAR) satellites like TerraSAR-X and TanDEM-X, it is now possible to map urban areas from space in very high level of detail using advanced interferometric techniques such as persistent scatterer interferometry and tomographic SAR inversion (TomoSAR), whereas these multi-pass techniques are based on a great number of images. We aim at precise TomoSAR reconstruction while significantly reducing the required number of images by incorporating building *a priori* knowledge to the estimation. In the paper, we propose a novel workflow that marries the freely available geographic information systems (GIS) data (i.e., 2-D building footprints) and the joint sparsity concept for TomoSAR inversion. Experiments on bistatic TanDEM-X data stacks demonstrate the great potential of the proposed approach, e.g., highly accurate tomographic reconstruction is achieved using six interferograms only.

Index Terms—Compressive sensing, GIS, joint sparsity, SAR tomography, synthetic aperture radar, TanDEM-X.

I. INTRODUCTION

MODERN spaceborne synthetic aperture radar (SAR) sensors, such as TerraSAR-X, TanDEM-X and COSMO-SkyMed, deliver SAR data with very high spatial resolution (VHR) of up to 1 m. With these meter resolution data, advanced multi-pass interferometric techniques such as persistent scatterer interferometry (PSI) and tomographic SAR inversion (TomoSAR) allow retrieving not only the 3-D geometrical shape but also the undergoing motion in the scale of millimeter of individual buildings [1]–[7]. In particular, sparse reconstruction based methods [8], [9], like SLIMMER [10], give robust TomoSAR inversion with very high elevation

resolution, and can offer so far ultimate 3-D, 4-D and 5-D SAR imaging [11], [12].

The downside of advanced repeat-pass InSAR techniques [13]–[20], like PSI and TomoSAR, are their high demand on data, i.e., typically a stack of 20–100 images over the illuminated area are required. For instance, it is demonstrated in [10] that by using even the most efficient algorithms, like non-linear least squares (NLS) and SLIMMER, a minimum number of 11 acquisitions are required to achieve a reasonable reconstruction in the interesting parameter range of spaceborne SAR. “Reasonable” in this context means that given an average signal-to-noise ratio (SNR) of 6 dB, the detection rate of double scatterers with an elevation distance of one Rayleigh resolution unit reaches at least 90%. However, if we can extract certain detailed features or patterns of high-rise buildings in SAR images, the required number of images can be significantly reduced by incorporating such features as prior for a joint estimation.

For this purpose, we propose a novel workflow marrying the globally available (2-D building footprint) GIS data and the joint sparsity concept for TomoSAR inversion, both of which have not yet been addressed in the community so far. Within this workflow, our main contributions are as follows:

- A robust procedure is proposed to use online freely assessable 2-D building footprints for extracting detailed high-rise building features including building masks, orientation, and iso-height lines (defined in [21]) in SAR image stacks (see Section III);
- The M-SLIMMER algorithm is proposed to promote joint sparsity for tomographic inversion of the identified iso-height pixel groups (see Section IV);
- By means of simulated data, the performance of M-SLIMMER is systematically evaluated in terms of elevation estimation accuracy, detection and false alarm rate of separating overlaid double scatterers, and its super-resolution capability. Compared to the single-snapshot sparsity model, as used in SLIMMER, the superior performance of the proposed joint sparsity approach is evident for all above mentioned quantitative metrics (see Section V);
- The first tomographic reconstruction using bistatic TanDEM-X data stacks is presented. The superior performance of M-SLIMMER is demonstrated in practice, e.g., highly accurate tomographic reconstruction is achieved using six interferograms only (see Section VI).

II. DATA SET

We work with 21 bistatic interferograms acquired by the German SAR satellites TerraSAR-X and TanDEM-X, with

Manuscript received January 29, 2015; revised June 02, 2015; accepted July 24, 2015. Date of publication August 18, 2015; date of current version November 17, 2015. This work was supported in part by the Helmholtz Association under the framework of the Young Investigators Group “SiPEO” (VH-NG-1018, www.sipeco.bgu.tum.de) and in part by the International Graduate School of Science and Engineering, Technische Universität München (Project 6.08: “4D City”). The guest editor coordinating the review of this manuscript and approving it for publication was Prof. Xiaopeng Yang.

X. X. Zhu is with the Remote Sensing Technology Institute (IMF), German Aerospace Center (DLR), 82234 Wessling, Germany, and also with Signal Processing in Earth Observation (SiPEO), Technische Universität München, 80333 Munich, Germany (e-mail: xiao.zhu@dlr.de).

N. Ge is with the Remote Sensing Technology Institute (IMF), German Aerospace Center (DLR), 82234 Wessling, Germany (e-mail: nan.ge@dlr.de).

M. Shahzad is with the Signal Processing in Earth Observation (SiPEO), Technische Universität München, 80333 Munich, Germany (e-mail: mohammad.shahzad@tum.de).

Color versions of one or more of the figures in this paper are available online at <http://ieeexplore.ieee.org>.

Digital Object Identifier 10.1109/JSTSP.2015.2469646

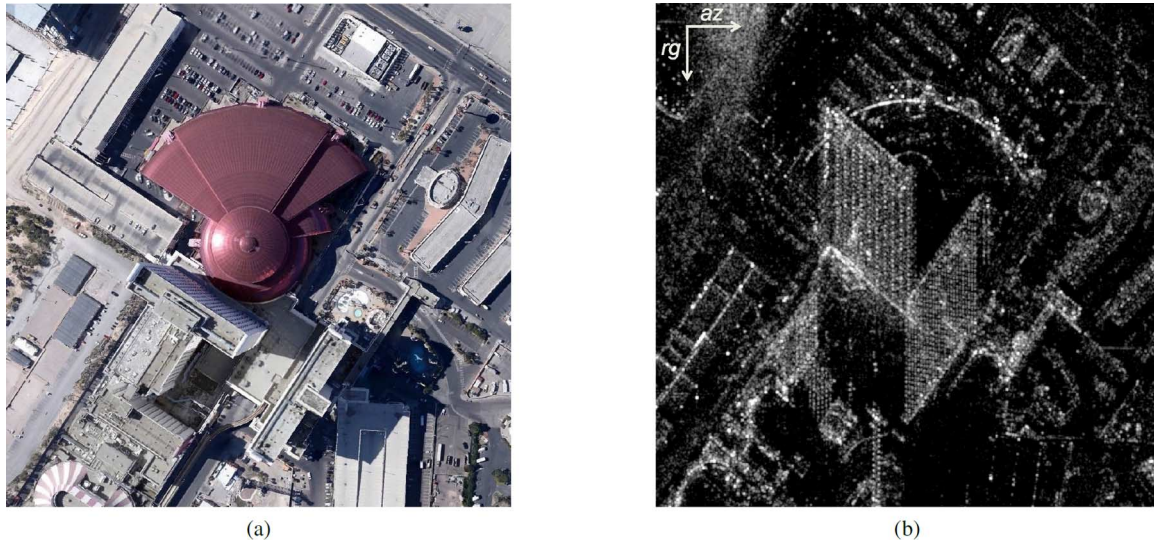


Fig. 1. Test Area: (a) Optical image of the test area ©Google; (b) Corresponding SAR intensity map (rg and az refer to range and azimuth directions, respectively).

cross-track baselines ranging between approximately ± 200 [m]. The single-pass characteristic renders atmospheric effects very small and deformation negligible. For this reason these datasets are ideal to test our proposed methodology. An optical image of the test area is shown in Fig. 1(a) while the corresponding SAR mean intensity image is shown in Fig. 1(b).

III. PRIOR KNOWLEDGE RETRIEVAL

In order to retrieve prior information pertaining to building regions, the 2-D building footprints are downloaded from OpenStreetMap (OSM). Based on the concept of crowd sourcing that involve crowd or community to effectively and efficiently fulfill a task at hand, OSM with around 2 million registered users (as of today and also rapidly growing) is considered to be the most successful Volunteered Geographic Information (VGI) project [22], [23]. The OSM database contains multitude of building footprints represented as polygons with ordered list of nodes/vertices (i.e., pairs of UTM or latitude/longitude coordinates according to WGS 84 coordinate system) and is updated every day. The data are free to download and comes under the open license Open Data Commons Database License (ODbL). Since it is a VGI project, the data quality may vary from region to region. To this end, the first investigations regarding OSM data quality were carried out for roads [24] followed by assessment of other attributes present in the database e.g., lines [25], polygonal objects [26] etc. Recently, the building footprints have also been evaluated for their completeness [27] and correctness [23]. The analysis of OSM data with surveying datasets reveals fairly precise positioning accuracies varying within 4 meters [23], [24]. The completeness percentage is already very high for many cities in Europe and US and is consistently increasing with time. Available 2-D footprints of the buildings in the city of Las Vegas are shown in Fig. 2 to give the reader an insight of the existing database. The high availability of such type of data triggers us to change our perspective of thinking, namely, instead of using Earth observation (EO) satellite data to build-up sources of geo-information for open users, we can explore the knowledge provided by social media to support information retrieval

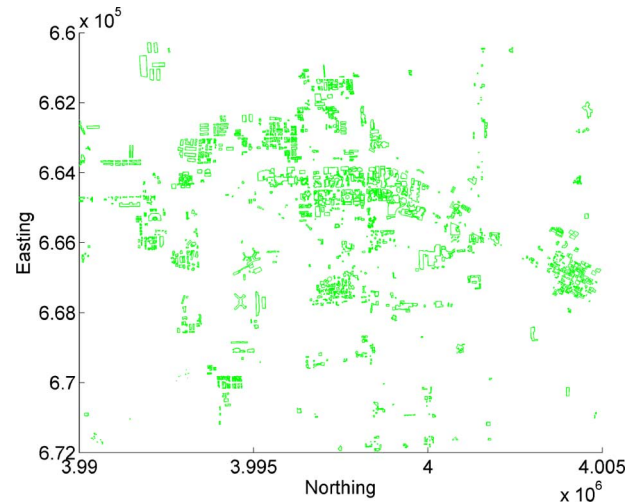


Fig. 2. GIS data (2-D building footprints) of Las Vegas from OSM.

from EO data. In this regard, one mission of this work is to demonstrate this concept in tomographic SAR reconstruction.

A. Automatic Extraction of Building Mask in SAR Image

The key idea is to make use of the aforementioned online freely assessable 2-D building footprints to extract detailed high rise building features including building masks, orientations, and the iso-height lines in SAR image data stacks. The extracted information can be further incorporated as a prior knowledge into the estimation for a more accurate tomographic SAR inversion. For this purpose, in this section we propose a sophisticated approach that is tolerable to moderate errors in the input GIS data for automatic extraction of aforementioned high rise building features in the SAR image data stacks:

- First the available building footprints from OpenStreetMap in world (latitude/longitude) coordinates are transformed/geo-coded into SAR (azimuth/range) imaging coordinate system. Fig. 3(a) shows the resulting projected reference polygons overlaid onto the buildings of interest in the corresponding SAR image shown in Fig. 1;

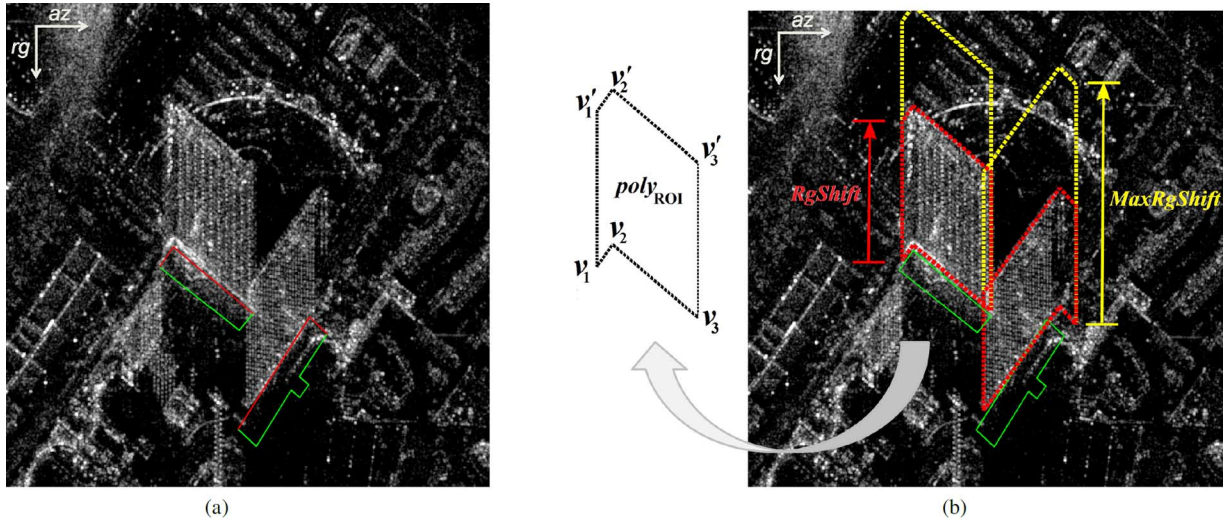


Fig. 3. Building mask extraction: (a) Reference polygons (shown in red and green polylines) of two buildings in the area of interest overlaid onto the SAR intensity map after geocoding. Side of the buildings facing the sensor are shown in red while the other side not visible to the sensor in green; (b) After rotation and range-azimuth shift compensation, the red polylines in (a) are shifted towards the sensor. The yellow dotted lines indicate the maximum range shift of $MaxRgShift$ (= 595 m) where as the red dotted lines indicate the $RgShift$ obtained by the proposed procedure in Algorithm 1.

- Secondly, due to the side looking geometry, SAR illuminates only one side of the building. Therefore, the complete building footprint of individual buildings is further segmented into two parts by means of a simple 2-D visibility test: 1) the part illuminated by the sensor which will be further used for iso-height pixel extraction (as depicted by red polylines in Fig. 3(a)); 2) the part in the shadow area not visible to the sensor which will not be used in further processing (as depicted by green polylines in Fig. 3(a));
- Finally, errors in the identified red polylines, caused by inaccuracies of the input GIS data in both orientation and translation, are compensated and the mask of individual buildings is further generated by iteratively shifting the corrected polylines towards the sensor.

In this regard, the approach depicted in Algorithm 1 is adopted. After transforming the available building footprints from world coordinates to SAR imaging coordinate system, we identify the side of the building footprint facing the SAR sensor as follows. If we assume that $v_{i=1, \dots, n}$ denote the indices of ordered 2-D footprint vertices of one particular building. Then any vertex v_k ($k \in n$) belongs to the side facing the sensor if and only if its projection onto the line at zeroth range axis (i.e., line defined as $rg = 0$ with zero azimuth slope) does not self-intersect the reference polygon. The range of total number of vertices belonging to the side visible to the sensor in any footprint is m where $1 < m \leq n$. The inequality that $m > 1$ depicts that, if not occluded, at least one side or two vertices of the building are always visible to the side looking SAR sensor.

Once the vertices facing to the sensor are identified, the step 3 in Algorithm 1 compensates for any positioning inaccuracy in the OSM footprint of the building in the area of interest. Possible error in OSM footprint is compensated by adopting the following sequence of steps:

- 1) Shift/translate the identified polyline in 2-D sliding window fashion within the intervals: range shift $[-10 \ 10]$ and azimuth shift $[-5 \ 5]$;

Algorithm 1 Procedure to automatically generate mask (or ROI) of an individual building

Require: 2-D polygonal footprint vertices $v_{i=1, \dots, n}$ in SAR coordinates of one particular building & SAR image of the scene.

- 1: Initialize: $MaxRgShift := 595$ and $d := 1$
 - 2: Identify the polyline comprising of m out of n vertices belonging to the building side facing the sensor
 - 3: Apply orientation correction and range-azimuth shift compensation to the identified polyline in order to cope for any positioning inaccuracy in the OSM footprint of the building
 - 4: **while (1) do**
 - 5: Shift/translate (in range direction) the polyline after orientation correction and azimuth-range compensation towards the sensor by distance d
 - 6: Compute the intensity values along the shifted polyline. This is accomplished by selecting equally spaced points along the shifted polyline, and then using nearest neighbor interpolation to find the intensity value for each point
 - 7: Take the median of computed intensity values along the shifted polyline and store the result in a column matrix $C(d, 1)$
 - 8: **if** $d == MaxRgShift$ **then**
 - 9: *break*
 - 10: **else**
 - 11: $d := d + 1$
 - 12: **end if**
 - 13: **end while**
 - 14: Take approximate derivative of C (i.e., calculate differences between adjacent elements of C), and store the result in matrix D
 - 15: Compute $\arg \max_{RgShift} (D_{RgShift})$ where $RgShift (= 1, \dots, d - 1)$ denotes the maximum change point in D
 - 16: Use $RgShift$ and m vertices of the identified (compensated) polyline facing the sensor to extract $poly_{ROI}$ of the particular building
-

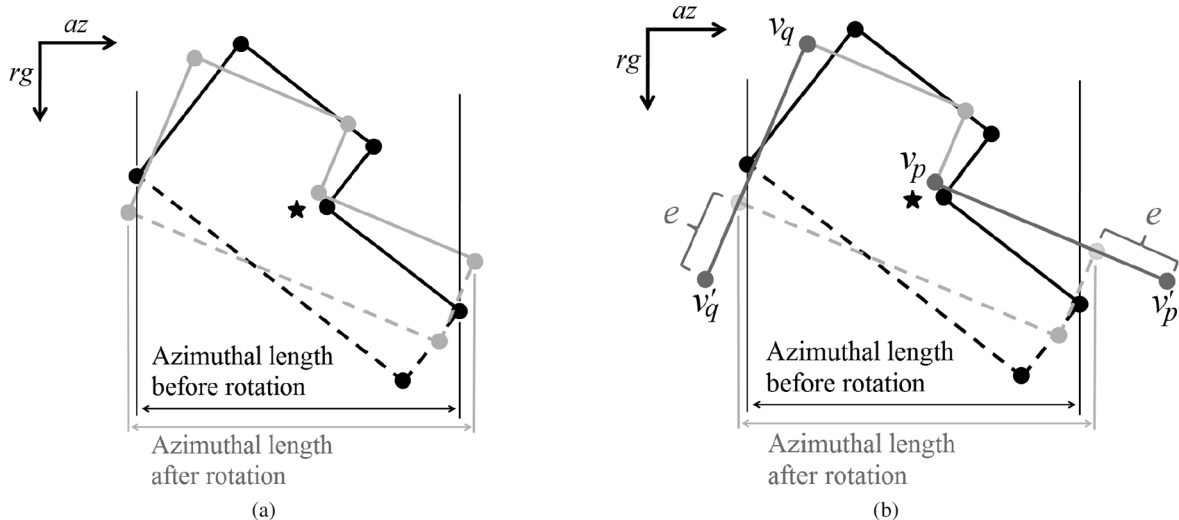


Fig. 4. Graphical illustration of adjusting polyline length: (a) Black and gray polygons indicate polygons before and after rotation (around centroid depicted as black star) respectively with circles representing the corresponding vertices. The dotted polylines represent building side not visible to the sensor. It is shown that after rotation the azimuthal length is changed; (b) The length of the outer (first and last edge depicted in dark gray) edges of the polyline facing the sensor is slightly extended by distance e ($= 5$ m in this work). Intensities (interpolated) over these extended edges are analyzed and first and last extended points (i.e., v'_p and v'_q) are respectively replaced by the points on the edges $v_p v'_p$ and $v_q v'_q$ where the approximate derivative (or change in intensities) is maximum.

- 2) Within each shift, rotate the polyline between interval $[-7.5 \ 7.5]$ degrees and compute median of intensities along the rotated polyline (similar to steps 6–7 in Algorithm 1);
- 3) The polyline is rotated and shifted with the rotation angle and the azimuth-range shifts which give the maximum of computed median intensities (from the previous step);
- 4) Finally, the rotation causes the change in the azimuthal length of the polyline which needs to be adjusted (see Fig. 4(a)). This is accomplished by first slightly extending the polyline and later adjusting the lengths of the outer (first and the last) edges of the polyline by analyzing their (interpolated) intensities (same as step 2 except that only the first and last edge of the polyline is used). Fig. 4(b) graphically illustrates the adjustment procedure.

In our experiment, the shifting intervals used in compensation are based on already mentioned 4 m inaccuracy of OSM data i.e., considering 4m inaccuracy, approx. range and azimuth resolution of 0.588m and 1.1 m requires range and azimuth shifts of atmost $(4/0.588 \approx) 6.8$ pixels and $(4/1.1 \approx) 3.6$ pixels.

After compensating any orientation and/or shifting inaccuracies, steps 4 to 13 in Algorithm 1 iteratively shifts the compensated polyline towards the sensor (in range direction only). Since the tallest building in the city of Las Vegas, the Stratosphere Tower, is around 350 m, $MaxRgShift$ in Algorithm 1 is set to 595 i.e., maximum building size along elevation appearing in the SAR image of Las Vegas city, computed as $350/0.588 (\approx 595)$ pixels where 0.588 m is the approx. range resolution. Thus the polyline is shifted till $MaxRgShift$ and the column vector C stores the median of computed intensity values along each range shift. Steps 14 and 15 in Algorithm 1 then computes the maximum change point $RgShift$ in the approximate derivative of C . $RgShift$ is then used in step 16 to determine $poly_{ROI}$ which describes the polygon surrounding the overlaid pixels of the same building in the SAR image. To elaborate how $poly_{ROI}$

is computed, consider a building having three adjacently connected vertices $v_1 - v_2 - v_3$ of the polyline facing the sensor where—denotes the adjacency (i.e., v_2 is adjacently connected to v_1 and v_3 , and so on). Assuming that the polyline has been compensated for rotation and range-azimuth shifts, the $poly_{ROI}$ is then simply formed as $v_1 - v_2 - v_3 - v'_3 - v'_2 - v'_1 - v_1$ where $\mathbf{v}'_j(az, rg) = \mathbf{v}_j(az, rg - RgShift)$ with $j = 1, 2, 3$ (see Fig. 3(b)). Finally, $poly_{ROI}$ is used to generate the building mask of an individual building.

B. Pixel Grouping

Based on the extracted masks of individual buildings, pixels sharing similar heights are then grouped together. This procedure is done in three steps:

- 1) Iso-height lines will be reproduced by translating the adjusted polyline towards both ends of the building mask with sub-pixel step size;
- 2) The distance between each pixel and its adjacent iso-height lines will be calculated;
- 3) Each pixel will be assigned to the closest iso-height line.

The distance between a pixel and an iso-height line is defined as the minimum absolute amount of translation (in pixels) towards or away from sensor. Fig. 5 illustrates one exemplary iso-height line in the cropped intensity image, as well as the final results of pixel grouping with each group of pixels plotted with a random color. Note that the color-coding already gives a rough idea about monotonic height change of the investigated façades.

IV. JOINT SPARSITY IN TOMOSAR

In this section, we first revisit a data model commonly used in TomoSAR, as well as the SLIMMER algorithm. Following this, we extend the SLIMMER algorithm for the multiple-snapshot case. The extended version exploits joint sparsity and is named as M-SLIMMER.

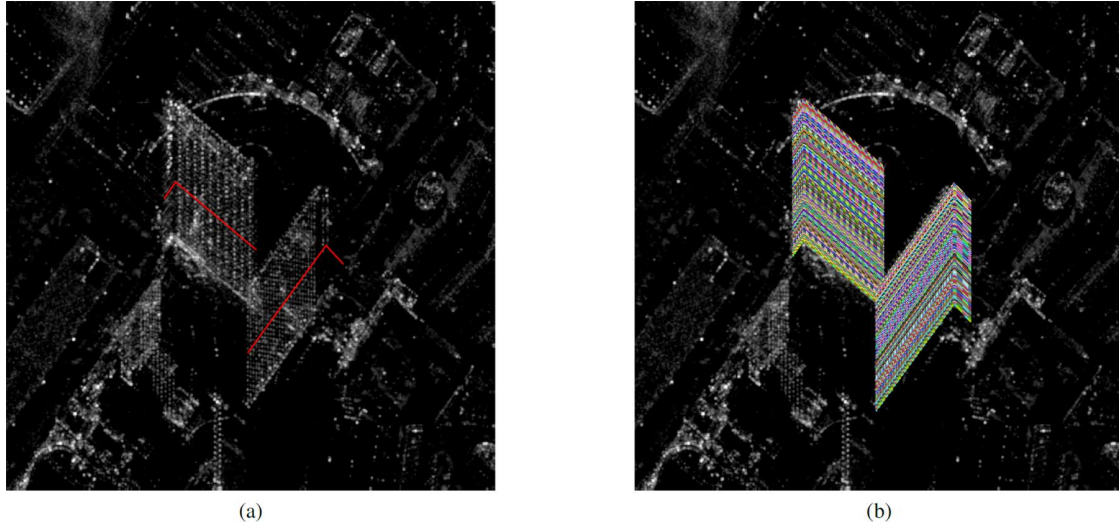


Fig. 5. Illustration of pixel grouping with (a) exemplary iso-height lines, and (b) grouped iso-height pixels color-coded with group indices.

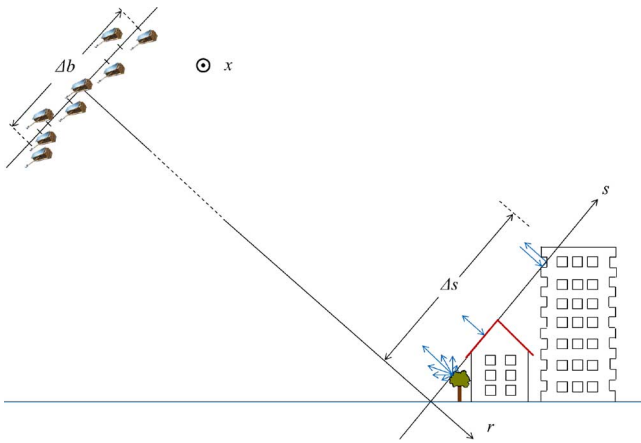


Fig. 6. TomoSAR imaging geometry with an artistic view of TerraSAR-X/TanDEM-X ©DLR. The satellite flies into the plane and looks to its right.

A. TomoSAR System Model

For a single SAR image, information along the third dimension, the so-called elevation axis s , which is perpendicular to the azimuth-range ($x-r$) plane, is integrated (see Fig. 6). I.e., echoes from, e.g., tree crown, building roof, or double-bounce effects on a balcony sharing the same distance to the sensor, are mapped onto one single pixel. To reconstruct reflectivity along s and to further separate those different contributions, TomoSAR utilizes scenes acquired from slightly different viewing angles to synthesize an elevation aperture Δb (cf. aperture along x created by steering the radar beam) for full 3-D SAR imaging [28]. A well-established model, which can be found, e.g., in [29], approximates each pixel value g_n as follows:

$$g_n = \int_{\Delta s} \gamma(s) \exp(-j2\pi\xi_n s) ds, \quad (1)$$

which is essentially the Fourier transform of the reflectivity function $\gamma(s)$ sampled at the spatial (elevation) frequency $\xi_n = -2b_n/(\lambda r)$, Δs is the elevation extent and λ is wavelength. Note that a possible motion term has been neglected here without loss of generality. For differential SAR tomography that takes into account the motion component, the readers are recommended to consult [17], [30], [31].

Discretizing the continuous reflectivity function in (1) along elevation s into L elevation positions $s_l \forall l \in \{1, \dots, L\}$, replacing integral by sum and taking into account measurement noise yield the following discrete system model:

$$\mathbf{g} = \mathbf{R}\boldsymbol{\gamma} + \boldsymbol{\varepsilon}, \quad (2)$$

where $\mathbf{g} \in \mathbb{C}^{N \times 1}$ is the measurement vector with $g_n \forall n \in \{1, \dots, N\}$, $\mathbf{R} \in \mathbb{C}^{N \times L}$ is an irregularly sampled Fourier transform matrix with $R_{nl} = \exp(-j2\pi\xi_n s_l)$, $\boldsymbol{\gamma} \in \mathbb{C}^{L \times 1}$ is the discretized reflectivity vector with $\gamma_l = \gamma(s_l) \forall l \in \{1, \dots, L\}$, and $\boldsymbol{\varepsilon} \in \mathbb{C}^{N \times 1}$ is additive noise which can be modeled as a zero-mean circular Gaussian random process. Typically we have $N \ll L$, which renders (2) underdetermined.

Similar to the resolution in azimuth, the Rayleigh resolution ρ_s is inversely proportional to the aperture size [2]

$$\rho_s = \frac{\lambda r}{2\Delta b}. \quad (3)$$

For high resolution spotlight data of TerraSAR-X/TanDEM-X, ρ_s is much worse than azimuth and range resolution (approx. 1.10 and 0.588 m, respectively) due to tight orbit control and amounts to about 24.9 m for our test data set.

B. The SLIMMER Algorithm

To solve (2), an algorithm called SLIMMER, which stands for Scale-down by L_1 norm Minimization, Model selection, and Estimation Reconstruction, has been proposed to achieve promising super-resolution power while guaranteeing the efficiency [8], [10]. SLIMMER has been originally designed for TomoSAR in urban areas, under the assumption that there are only a few dominant scatterers (phase centers) along elevation axis within each azimuth-range pixel [2]. I.e., $\boldsymbol{\gamma}$ has merely K non-zero entries with typically $K \leq 4$. As its name suggests, this algorithm consists of the following three main steps.

1) *Scale-Down by L_1 Norm Minimization*: To exploit the sparse prior on $\boldsymbol{\gamma}$, we solve the following L_1 -regularized least squares problem

$$\hat{\boldsymbol{\gamma}} = \arg \min_{\boldsymbol{\gamma}} \left\{ \frac{1}{2} \|\mathbf{g} - \mathbf{R}\boldsymbol{\gamma}\|_2^2 + \lambda_K \|\boldsymbol{\gamma}\|_1 \right\}, \quad (4)$$

where λ_K is a hyperparameter balancing model error and the sparsity of $\boldsymbol{\gamma}$. (4) is known to deliver robust elevation estimates \hat{s}_l of dominant scatterers. Therefore, by identifying the most significant entries in $\hat{\boldsymbol{\gamma}}$ and choosing certain columns of \mathbf{R} accordingly, the dimension of the original problem in (2) can be downscaled by a large factor. However, solving (4) is prone to amplitude bias due to the L_1 norm relaxation. Moreover, outliers might appear when the required mathematical conditions of \mathbf{R} are not fully fulfilled as most of the engineering problems do [32]. These make the next two steps necessary.

2) *Model Selection*: The initial estimate $\hat{\boldsymbol{\gamma}}$ from (4) may contain artifacts, which falsifies its sparsity level. In order to detect and remove them, the goodness of fit of a model should be penalized by its complexity, so that overfitting of data can be avoided. Model selection can be regarded as the following optimization problem

$$\hat{K} = \arg \min_K \left\{ -2 \ln p(\mathbf{g} | \hat{\boldsymbol{\theta}}(K), K) + 2C(K) \right\}, \quad (5)$$

where $p(\mathbf{g} | \hat{\boldsymbol{\theta}}(K), K)$ is the likelihood function of \mathbf{g} given the estimates of unknown $\boldsymbol{\theta}(K)$ and K , $C(K)$ is the penalty term for model complexity. Various alternatives of $C(K)$ have been devised for different needs, e.g., Bayesian information criterion, Akaike information criterion, minimum description length, to name a few [33]. By choosing one specific criterion suitable for the given datasets, (5) is then solved as a combinatorial problem over a pre-defined range of K . Likewise, the most likely positions \hat{s} of non-zero elements in $\hat{\boldsymbol{\gamma}}$ will hereby be estimated, which further shrinks \mathbf{R} . This leaves only one last step to correct amplitude bias.

3) *Parameter Estimation*: At this stage, we have a much slimmer sensing matrix $\mathbf{R}(\hat{s}) \in \mathbb{C}^{N \times \hat{K}}$. This renders (2)

$$\mathbf{g} = \mathbf{R}(\hat{s})\boldsymbol{\gamma}(\hat{s}) + \mathbf{e}, \quad (6)$$

where $\boldsymbol{\gamma}(\hat{s}) \in \mathbb{C}^{\hat{K} \times 1}$, and $\mathbf{e} \in \mathbb{C}^{N \times 1}$ is the sum of measurement noise and the error introduced by model selection. Since (6) is now overdetermined, it can be solved with ordinary least squares (OLS)

$$\hat{\boldsymbol{\gamma}} = \mathbf{R}^+(\hat{s})\mathbf{g}, \quad (7)$$

where $(\cdot)^+$ denotes pseudoinverse.

Within the framework of SLIMMER, sparse reconstruction and OLS join forces to incorporate both robust identification of scatterers' elevation positions and accurate amplitude estimation. Other advantages of SLIMMER over conventional parametric and non-parametric methods have been discussed in [8] and its theoretical limits in terms of estimation accuracy, super-resolution power and the required minimum number of acquisitions for a reasonable reconstruction have been investigated in [10].

C. The M-SLIMMER Algorithm

We extend the SLIMMER algorithm to M-SLIMMER for the multiple-snapshot case. Assume that by applying the method described in Section III, we have already detected M pixels along an iso-height line. We further assume that within each pixel, there is a dominant scatterer located on a building façade.

Hence, those M scatterers should reside at the same height or elevation position. For each pixel, we have, similar to (2),

$$\mathbf{g}_m = \mathbf{R}_m \boldsymbol{\gamma}_m + \boldsymbol{\varepsilon}_m, \quad (8)$$

$\forall m \in \{1, \dots, M\}$. If the iso-height line stretches principally in azimuth direction, we expect ξ_n to vary little among all concerned pixels. For this reason, we define $\mathbf{R} := \mathbf{R}_1 \approx \mathbf{R}_2 \approx \dots \approx \mathbf{R}_M$. By using the identical degree of discretization along elevation axis, we can rewrite (8) as

$$\mathbf{G} = \mathbf{R}\boldsymbol{\Gamma} + \mathbf{E}, \quad (9)$$

where $\mathbf{G} = [\mathbf{g}_1, \dots, \mathbf{g}_M]$ is the measurement matrix with M snapshots, $\boldsymbol{\Gamma} = [\boldsymbol{\gamma}_1, \dots, \boldsymbol{\gamma}_M]$ is the unknown discretized reflectivity matrix, and \mathbf{E} accounts for both additive noise and possible model error. (9) is again an underdetermined system with $N \ll L$ which has infinitely many solutions. Since we assume that all the snapshots have one contribution from the same height on a façade, the non-zero entry positions in the columns of $\boldsymbol{\Gamma}$ are aligned in a row-wise fashion. This property of signals is also referred to as joint sparsity. Indeed, there can be more non-zero rows related to ground, lower infrastructures, building roof, etc. Still, the number of non-zero rows of $\boldsymbol{\Gamma}$ is very limited. To incorporate this prior, $\hat{\boldsymbol{\Gamma}}$ can be estimated by solving the following $L_{1,2}$ -regularized least squares problem [34],

$$\hat{\boldsymbol{\Gamma}} = \arg \min_{\boldsymbol{\Gamma}} \left\{ \frac{1}{2} \|\mathbf{G} - \mathbf{R}\boldsymbol{\Gamma}\|_F^2 + \lambda_K \|\boldsymbol{\Gamma}\|_{1,2} \right\}, \quad (10)$$

where F denotes the Frobenius norm, and the mixed norm $\|\boldsymbol{\Gamma}\|_{1,2} = \sum_{l=1}^L (\|\boldsymbol{\gamma}^l\|_2)$ promotes joint sparsity with $\boldsymbol{\gamma}^l$ being the l^{th} row of $\boldsymbol{\gamma}$. It has been shown in [35] that the probability of successful recovery increases with the number of snapshots. Note that different polarimetric channels or neighboring pixels were used in a similar way in [36], [37].

After solving (10), model selection and parameter estimation will be performed individually for each pixel as the SLIMMER algorithm does.

D. Cramér-Rao Lower Bounds (CRLB) for Elevation Estimates

The Cramér-Rao lower bound (CRLB) of elevation estimates \hat{s} for the single-scatterer case has been derived in [38] as

$$\sigma_{s,0} = \frac{\lambda r}{4\pi\sqrt{N} \cdot \sqrt{2\text{SNR}} \cdot \sigma_b}, \quad (11)$$

where σ_b is the standard deviation of b_n . Given an SNR of 3 dB, the CRLB is approx. 1.11 m with all 21 acquisitions.

In urban environment, due to the side-looking geometry of SAR, multiple scatterers are often mapped onto one azimuth-range pixel. The fact that closely spaced scatterers will interfere with each other renders a degraded estimation accuracy of individual scatterers [12]. In the interest of super-resolution, the CRLB for elevation estimate of the q^{th} ($q = 1, 2$) scatterer has been derived in [10] as

$$\sigma_{s_q} = c_0 \cdot \sigma_{s_q,0}, \quad (12)$$

where

$$c_0 \approx \max \left\{ \sqrt{2.57 (\alpha^{-1.5} - 0.11)^2 + 0.62}, 1 \right\} \quad (13)$$

is the interference factor depending on α which is the elevation distance between two scatterers normalized w.r.t. the Rayleigh resolution unit [10]. c_0 is equal to one (meaning no interference) when two scatterers are far apart, i.e., $\alpha \gg 1$, greater than one when two scatterers are closely spaced ($\alpha < 1.5$) and increasing with decreasing α .

V. PERFORMANCE EVALUATION USING SIMULATED DATA

In general, as an extension of SLIMMER, M-SLIMMER has the same basic principle. However, instead of exploiting sparsity in a single snapshot, M-SLIMMER uses multiple snapshots of iso-height pixels identified in SAR images (with the help of supporting OSM data). Since M-SLIMMER makes use of more measurements than SLIMMER, we naturally expect it to achieve better performance.

In this section, the performance of the proposed M-SLIMMER algorithm, including elevation estimation accuracy, detection rate and false alarm rate of separating overlaid scatterers, and its super-resolution capability, is evaluated using simulated data.

We simulate façade-ground interaction of two scatterers spaced by decreasing elevation distances, which is a well-known TomoSAR benchmark test [2], [8]. Note that we only work in the super-resolution regime, i.e., the elevation distance between façade and ground is no larger than the Rayleigh resolution ρ_s . Four scenarios are taken into account with the number of measurements $N \in \{6, 11\}$ and $SNR \in \{3, 10\}$ in [dB] because:

- As mentioned above, eleven is the minimum required number of measurements for a reasonable reconstruction in the interesting SNR range of spaceborne SAR if SLIMMER is used [10];
- In case of two scatterers, six is the number of unknowns, namely the amplitude, phase and elevation position of each scatterer;
- SNR of 3 dB and 10 dB are usually considered as the lower and upper bound of persistent scatterers, respectively [39].

For each façade-ground interaction with a given elevation distance, we independently generate $M = 48$ snapshots, which is an average case for the test buildings in Fig. 5. The true elevation of simulated façade and ground is shown as two solid line segments w.r.t. their normalized elevation distance $\delta\alpha$ in Fig. 7, respectively. In addition, we show for the case $N = 11$ the evolution of CRLB, which increases with decreasing elevation distance of two interfering scatterers in the super-resolution regime, as implied by (12) and (13). The dashed lines mark true elevation $\pm 1 \times \text{CRLB}$ with N interferograms, denoted as $\text{CRLB}(N)$, while we plot true elevation $\pm 1 \times \text{CRLB}$ with NM interferograms, denoted as $\text{CRLB}(NM)$, as dotted lines. We will show that M-SLIMMER using N interferograms and M snapshots approaches the latter bound, which can be achieved by SLIMMER given NM interferograms.

We solve the L_1 - and $L_{1,2}$ -regularized least squares problems independently, and then follow the SLIMMER procedures to perform model selection and parameter estimation. λ_K is chosen adaptively, which depends on L , M and the noise level of observations [34]. The results are shown in Figs. 8 and 9 with elevation estimates $\hat{\alpha}$ of façade and ground plotted w.r.t. their

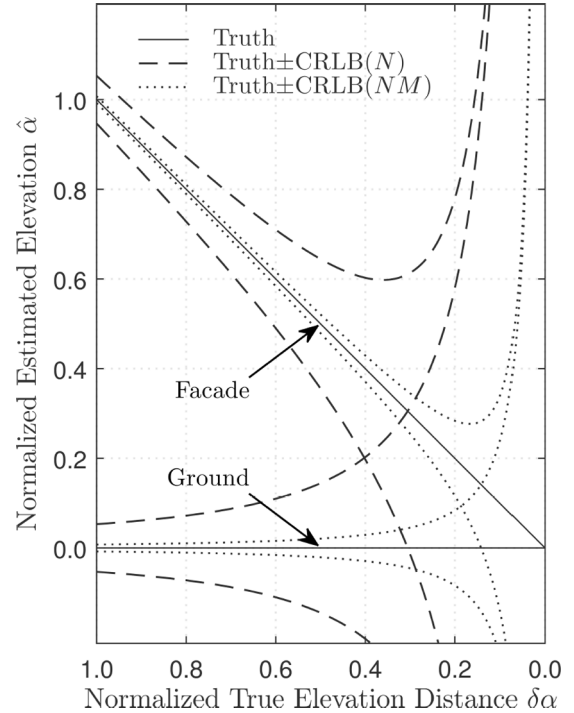


Fig. 7. Normalized true elevation α of simulated façade and ground (solid lines), as well as the CRLB of normalized elevation estimates, both w.r.t. normalized true elevation distance $\delta\alpha$. Dashed lines: CRLB with N baselines; dotted lines: CRLB with NM baselines.

normalized true elevation difference $\delta\alpha$. Each dot depicts mean value of all estimates, with error bar indicating its standard deviation. In each subplot, the two solid line segments mark the true elevation for façade and ground, respectively, while the dashed and dotted lines denote true elevation $\pm 1 \times \text{CRLB}$, which is the same as in Fig. 7. Missing points suggest that detection rate is below 25%. Note that we define detection for the case when not only two scatterers are separated, but also their estimates should be bounded by $\pm 3 \times \text{CRLB}(N)$ of their true elevation. For $N = 11$, the elevation estimates with both methods are still somewhat comparable, despite the fact that joint sparsity model leads to much smaller variance and slightly better super-resolution capability. SLIMMER performs in particular worse with smaller N and lower SNR. On the contrary, even for the case $N = 6$, reasonable elevation has been reconstructed with M-SLIMMER. It is worth mentioning that M-SLIMMER with N interferograms and M snapshots is equivalent to SLIMMER with NM measurements in relation to the standard deviation of elevation estimates, although the mean values slowly drift away from the true elevation due to the increasing interference between two scatterers.

In Fig. 10, the detection rate P_D is provided for the case $N = 11$ w.r.t. normalized true elevation distance $\delta\alpha$. The red and blue colors denote M-SLIMMER and SLIMMER, respectively. The solid and dashed lines illustrate the results with $SNR = 10$ dB and 3 dB, respectively. If we define elevation resolution to be the minimum distance between façade and ground required to achieve at least 50% detection rate, then the resolution of M-SLIMMER is approximately one tenth of Rayleigh resolution better than the one of SLIMMER, given

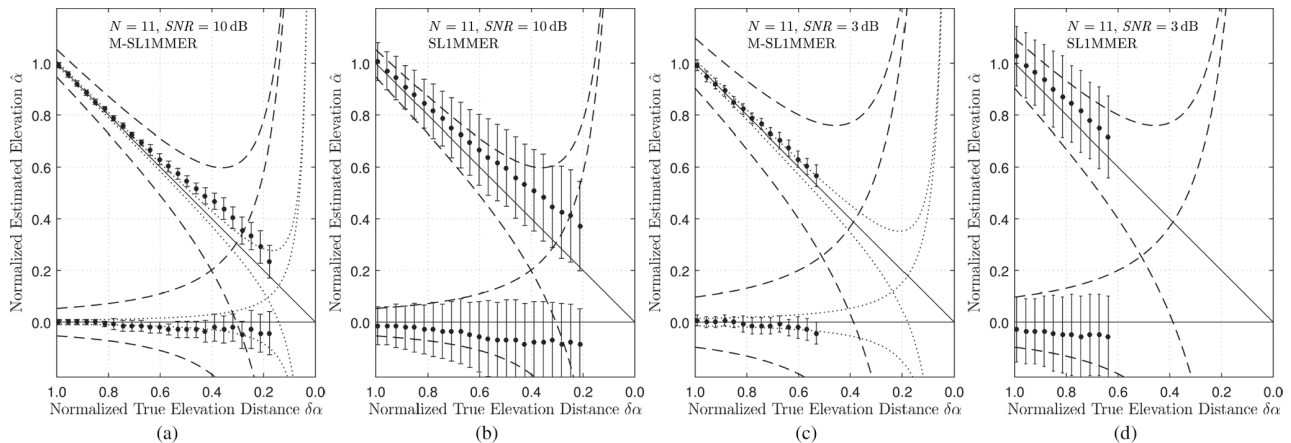


Fig. 8. Reconstructed elevation of simulated façade and ground with $M = 48$, $N = 11$: (a) $SNR = 10$ dB with M-SLIMMER, (b) $SNR = 10$ dB with SLIMMER, (c) $SNR = 3$ dB with M-SLIMMER, and (d) $SNR = 3$ dB with SLIMMER respectively. Each dot has the sample mean of all estimates as its y value and the corresponding standard deviation as error bar.

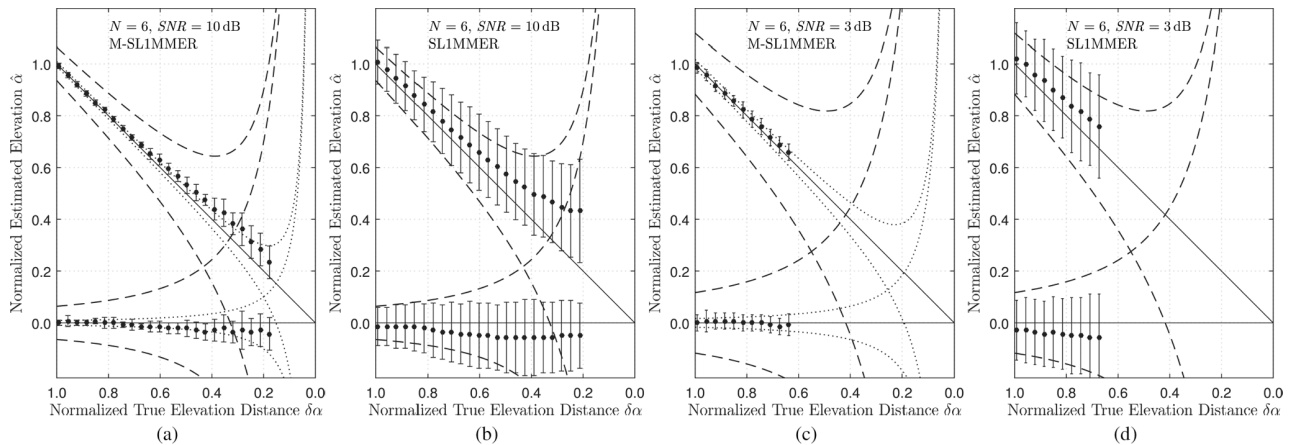


Fig. 9. Reconstructed elevation of simulated façade and ground with $M = 48$, $N = 6$, (a) $SNR = 10$ dB with M-SLIMMER, (b) $SNR = 10$ dB with SLIMMER, (c) $SNR = 3$ dB with M-SLIMMER, and (d) $SNR = 3$ dB with SLIMMER, respectively. Each dot has the sample mean of all estimates as its y value and the corresponding standard deviation as error bar.

an SNR of 10 dB before. We also analyzed P_D w.r.t. SNR for two typical elevation distances $\alpha = 1$ or 0.4 , i.e., when two scatterers are spaced by one or two fifths of Rayleigh resolution. The results are shown in Fig. 11(a). Moreover, false alarm rate P_F is illustrated in Fig. 11(b) as a function of SNR for M-SLIMMER (red) and SLIMMER (blue), respectively. In this context, we simulate only one scatterer and define false alarm for the case when two scatterers are detected. These analyses confirm the fact that M-SLIMMER outperforms SLIMMER in all respects significantly. For the case $N = 6$, the gain of using multiple snapshots regarding P_D and P_F is comparable to the case of $N = 11$.

VI. PRACTICAL DEMONSTRATION USING TANDEM-X DATA

In this section, M-SLIMMER is applied to the TanDEM-X data mentioned in Section II. The results are compared to those obtained using SLIMMER. Figs. 12–14 show the reconstructed and color-coded elevation of the two test buildings in Fig. 5, overlaid with intensity. From Fig. 12 to Fig. 14, 21, 11 and 6 interferograms are used, respectively. The separated scatterers, from left to right estimated using M-SLIMMER and SLIMMER and from top to down of first and second layer, are illustrated respectively.

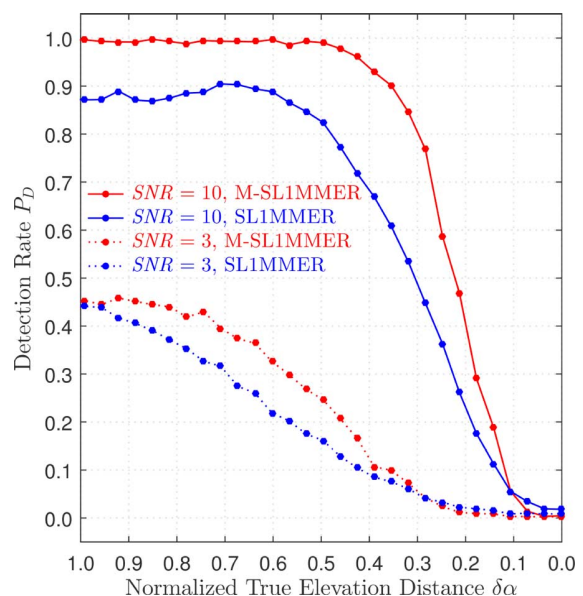


Fig. 10. Detection rate P_D w.r.t. normalized true elevation distance $\delta\alpha$ between façade and ground, for the case $N = 11$. Red solid: $SNR = 10$ dB with M-SLIMMER, blue solid: $SNR = 10$ dB with SLIMMER, red dotted: $SNR = 3$ dB with M-SLIMMER, blue dotted: $SNR = 3$ dB with SLIMMER, respectively.

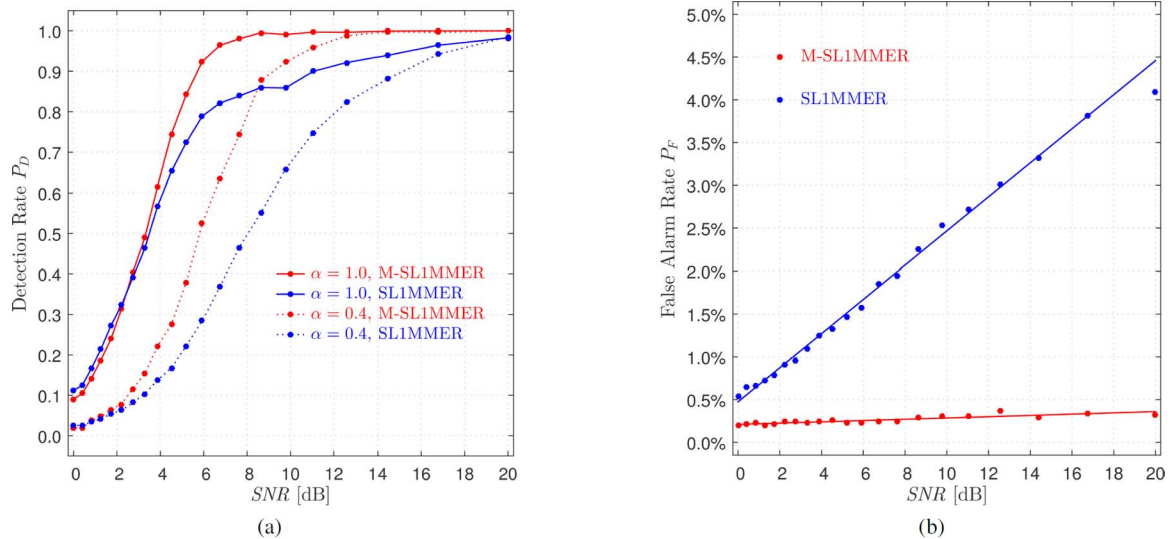


Fig. 11. Detection rate P_D and false alarm rate P_F w.r.t. SNR , for the case $N = 11$. (a) P_D for $\alpha = 1.0$ with M-SLIMMER (red solid), $\alpha = 1.0$ with SLIMMER (blue solid), $\alpha = 0.4$ with M-SLIMMER (red dotted), and $\alpha = 0.4$ with SLIMMER (blue dotted), respectively. (b) P_F with M-SLIMMER (red), and SLIMMER (blue), respectively.

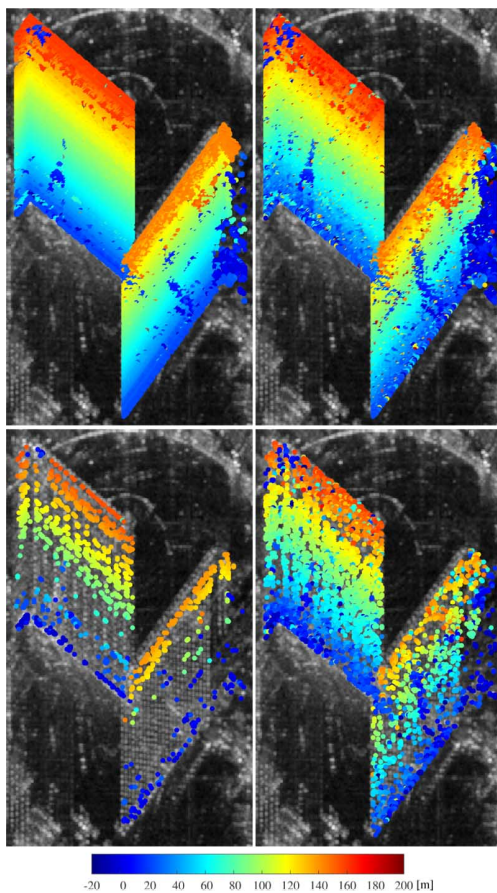


Fig. 12. Reconstructed and color-coded elevation of the two test buildings using 21 interferograms, visualized in two layers, overlaid with intensity. From top to down: first and second layer, respectively; from left to right: M-SLIMMER and SLIMMER, respectively.

At the top of the test buildings, reflections from building roof and façade are overlaid. In these practical examples, dominating scattering from roof (dark red) can be seen in the first layer, whereas the corresponding parts of façade (light red) are

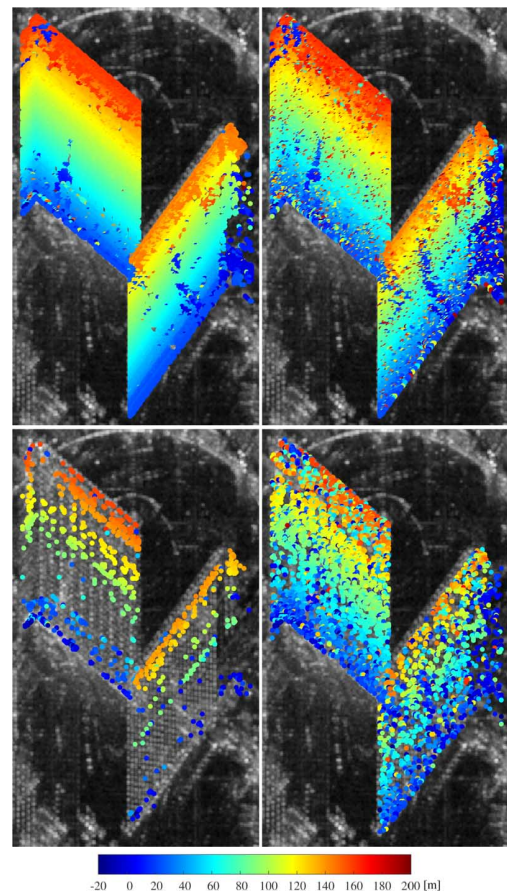


Fig. 13. The same results as Fig. 12, but using 11 interferograms.

visible in the second layer. We do not expect many reflections from lower structures though, due to the large slope of the shell-like roof in front of the test buildings. It is evident that M-SLIMMER (left) using joint sparsity model significantly outperforms SLIMMER (right). In particular, when $N = 6$, i.e., using extremely small number of scenes, the second layer estimated using SLIMMER (lower right plot of Fig. 14) is

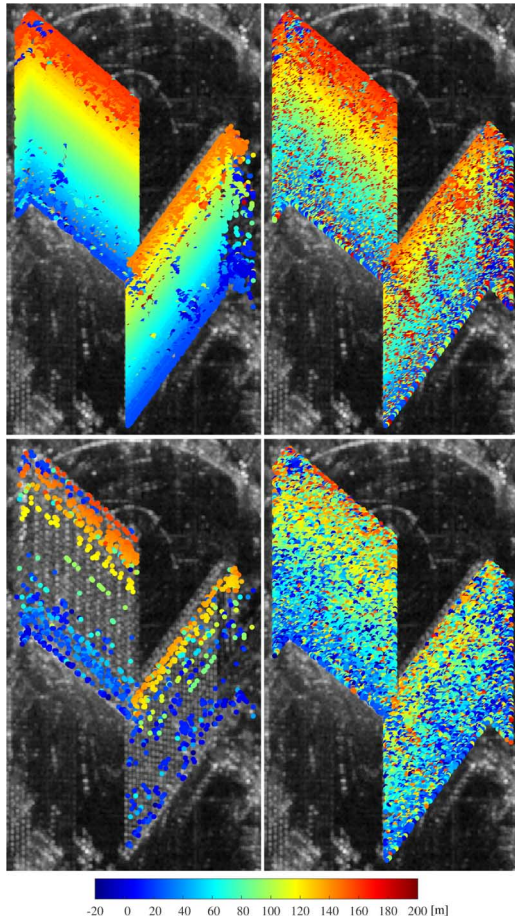


Fig. 14. The same results as Fig. 12, but using 6 interferograms only.

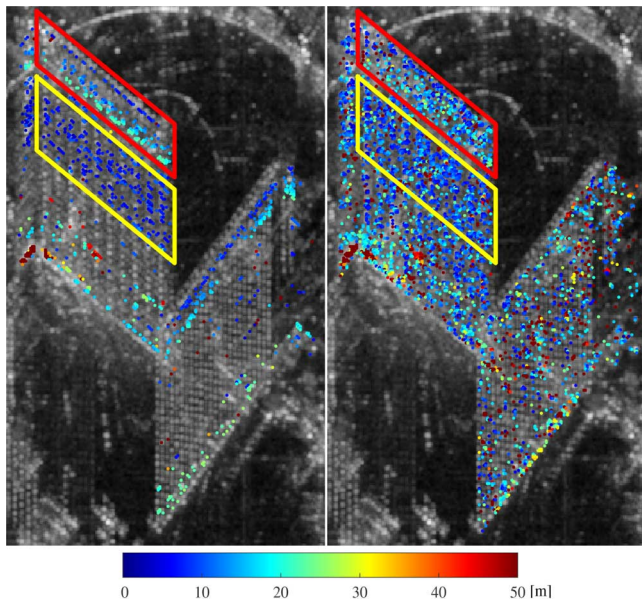


Fig. 15. Elevation distance between first and second layer with $N = 21$. Left: M-SLIMMER; right: SLIMMER.

deteriorated by false alarms while M-SLIMMER still achieves reasonable results (lower left plot of Fig. 14).

Due to the significantly improved estimation accuracy, M-SLIMMER reconstructs some interesting details which

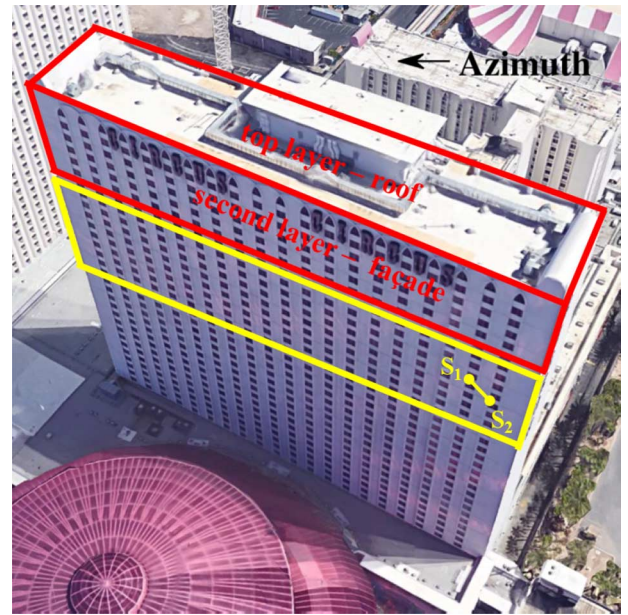


Fig. 16. Optical image of the left test building in Fig. 15 ©Google.

was not accessible so far. For a practical demonstration, we calculated elevation distance between first and second layer for the double-scatterer case, which is shown in Fig. 15. The red parallelogram marks the area where facade and roof are overlaid, cf. Fig. 16. At the far-range side of this area, the elevation distance amounts to approximately 22.60 [m] (cyan). Accordingly, the width of the roof can be calculated to be 18.27 [m], which agrees, up to the decimeter level, with what we estimated from the 3-D building model of Google Earth. Besides, the yellow parallelogram marks an area where the elevation distance between separated overlaid scatterers stays more or less constant. While comparing the SAR amplitude image to the optical one in Fig. 16, a plausible explanation is that two neighboring windows in the diagonal direction exemplified as S_1 and S_2 , are superimposed. As can be counted from Fig. 16, the number of windows per floor adds up to 20, whereas there are only 10 extraordinarily bright pixels in the SAR amplitude image. However, this speculation needs to be further verified using SAR simulation tools providing a highly precise building model.

VII. CONCLUDING REMARKS

In this paper, a novel framework is proposed which can achieve precise TomoSAR reconstruction while significantly reducing the required number of images. The core idea is the exploitation of joint sparsity in iso-height SAR pixel groups that can be identified with the support of online available GIS data—2D building footprints. Experiments using bistatic TanDEM-X data stacks demonstrate the great potential of the proposed approach.

A few additional remarks might be helpful for further use of our results:

- The approach we proposed for grouping iso-height pixels can also be used for all other estimators that support multiple-snapshot (also referred to as multi-look) estimation, like NLS, MUSIC, etc.;

- Our experiments are performed over Las Vegas where GIS data of moderate quality are available. For test areas with relatively poor 2-D footprint data, the benefit of the proposed approach that refines the iso-height lines of each building using, e.g., SAR intensity map, could be even more evident;
- In the cities where GIS data are not available, one can use the 2-D footprint reconstructed using a preliminarily retrieved TomoSAR point cloud [40] to alternately improve the TomoSAR estimation procedure;
- The proposed M-SLIMMER is a general spectral estimator, even though we applied it here for tomographic reconstruction;
- In our work, the mixed $L_{1,2}$ norm is introduced to promote the joint sparsity prior. Depending on the applications, this constraint can be relaxed by replacing $L_{1,2}$ with $L_{p,2}$ norm with $p > 1$;

In the future, we will extend the proposed M-SLIMMER for higher dimensional spectral estimation problems, e.g., differential tomographic SAR reconstruction using mixed single- and multi-pass monostatic data stacks.

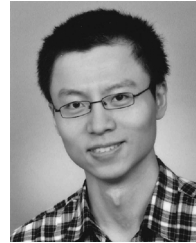
REFERENCES

- [1] S. Gernhardt, N. Adam, M. Eineder, and R. Bamler, "Potential of very high resolution SAR for persistent scatterer interferometry in urban areas," *Ann. GIS*, vol. 16, no. 2010-06, pp. 103–111, 2010.
- [2] X. X. Zhu and R. Bamler, "Very high resolution spaceborne SAR tomography in urban environment," *IEEE Trans. Geosci. Remote Sens.*, vol. 48, no. 12, pp. 4296–4308, Dec. 2010.
- [3] D. Reale, G. Fornaro, A. Pauciuolo, X. Zhu, and R. Bamler, "Tomographic imaging and monitoring of buildings with very high resolution SAR data," *IEEE Geosci. Remote Sens. Lett.*, vol. 8, no. 4, pp. 661–665, Jul. 2011.
- [4] G. Fornaro, A. Pauciuolo, D. Reale, X. Zhu, and R. Bamler, "SAR tomography: An advanced tool for 4d spaceborne radar scanning with application to imaging and monitoring of cities and single buildings," *IEEE Geosci. Remote Sens. Newslett.*, pp. 10–18, 2012.
- [5] Y. Wang, X. X. Zhu, Y. Shi, and R. Bamler, "Operational TomoSAR processing using TerraSAR-X high resolution spotlight stacks from multiple view angles," in *Proc. IEEE Int. Geosci. Remote Sens. Symp. (IGARSS)*, 2012, pp. 7047–7050.
- [6] X. X. Zhu and M. Shahzad, "Facade reconstruction using multiview spaceborne tomoSAR point clouds," *IEEE Trans. Geosci. Remote Sens.*, vol. 52, no. 6, pp. 3541–3552, Jun. 2014.
- [7] G. Fornaro, F. Lombardini, A. Pauciuolo, D. Reale, and F. Viviani, "Tomographic processing of interferometric SAR data: Developments, applications, and future research perspectives," *IEEE Signal Process. Mag.*, vol. 31, no. 4, pp. 41–50, Jul. 2014.
- [8] X. X. Zhu and R. Bamler, "Tomographic SAR inversion by L1-norm regularization: The compressive sensing approach," *IEEE Trans. Geosci. Remote Sens.*, vol. 48, no. 10, pp. 3839–3846, Oct. 2010.
- [9] A. Budillon, A. Evangelista, and G. Schirinzi, "Three-dimensional SAR focusing from multipass signals using compressive sampling," *IEEE Trans. Geosci. Remote Sens.*, vol. 49, no. 1, pp. 488–499, Jan. 2011.
- [10] X. X. Zhu and R. Bamler, "Super-resolution power and robustness of compressive sensing for spectral estimation with application to spaceborne tomographic SAR," *IEEE Trans. Geosci. Remote Sens.*, vol. 50, no. 1, pp. 247–258, Jan. 2012.
- [11] X. X. Zhu and R. Bamler, "Demonstration of super-resolution for tomographic SAR imaging in urban environment," *IEEE Trans. Geosci. Remote Sens.*, vol. 50, no. 8, pp. 3150–3157, Aug. 2012.
- [12] X. X. Zhu and R. Bamler, "Superresolving SAR tomography for multidimensional imaging of urban areas: Compressive sensing-based tomoSAR inversion," *IEEE Signal Process. Mag.*, vol. 31, no. 4, pp. 51–58, Jul. 2014.
- [13] A. Ferretti, C. Prati, and F. Rocca, "Analysis of permanent scatterers in SAR interferometry," in *Proc. IEEE Int. Geosci. Remote Sens. Symp. (IGARSS)*, 2000, vol. 2, pp. 761–763.
- [14] B. M. Kampes, *Radar Interferometry: Persistent Scatterer Technique*. New York, NY, USA: Springer Science & Business Media, 2006.
- [15] N. Adam, B. Kampes, M. Eineder, J. Worawattanamateekul, and M. Kircher, "The development of a scientific permanent scatterer system," in *Proc. ISPRS Workshop High Resolut. Map. Space*, Hannover, Germany, 2003.
- [16] G. Fornaro, F. Lombardini, and F. Serafino, "Three-dimensional multipass SAR focusing: Experiments with long-term spaceborne data," *IEEE Trans. Geosci. Remote Sens.*, vol. 43, no. 4, pp. 702–714, Apr. 2005.
- [17] F. Lombardini, "Differential tomography: A new framework for SAR interferometry," *IEEE Trans. Geosci. Remote Sens.*, vol. 43, no. 1, pp. 37–44, Jan. 2005.
- [18] A. Ferretti, A. Fumagalli, F. Novali, C. Prati, F. Rocca, and A. Rucci, "A new algorithm for processing interferometric data-stacks: Squeasar," *IEEE Trans. Geosci. Remote Sens.*, vol. 49, no. 9, pp. 3460–3470, Sep. 2011.
- [19] Y. Wang, X. X. Zhu, and R. Bamler, "Retrieval of phase history parameters from distributed scatterers in urban areas using very high resolution SAR data," *ISPRS J. Photogram. Remote Sens.*, vol. 73, pp. 89–99, 2012.
- [20] M. Schmitt and U. Stilla, "Adaptive multilooking of airborne single-pass multi-baseline InSAR stacks," *IEEE Trans. Geosci. Remote Sens.*, vol. 52, no. 1, pp. 305–312, Jan. 2014.
- [21] R. Guo and X. X. Zhu, "High-rise building feature extraction using high resolution spotlight TanDEM-X data," in *Proc. 10th Eur. Conf. Synthetic Aperture Radar (EUSAR)*, Jun. 2014, pp. 1–4.
- [22] Stats—OpenStreetMap Wiki [Online]. Available: <http://wiki.openstreetmap.org/wiki/Statistics>
- [23] H. Fan, A. Zipf, Q. Fu, and P. Neis, "Quality assessment for building footprints data on OpenStreetMap," *Int. J. Geogr. Inf. Sci.*, vol. 28, no. 4, pp. 700–719, Apr. 2014.
- [24] M. Haklay, "How good is Volunteered geographical information? A comparative study of OpenStreetMap and ordnance survey datasets," *Environ. Planning B: Planning Design*, vol. 37, no. 4, pp. 682–703, 2010.
- [25] M. Helbich, C. Amelunxen, and P. Neis, "Comparative spatial analysis of positional accuracy of OpenStreetMap and proprietary geodata," in *Proc. AGILE'11*, Heidelberg, Germany, 2011, p. 69120, GIScience, Dept. of Geography, Univ. of Heidelberg.
- [26] P. Mooney, P. Corcoran, and A. C. Winstanley, "Towards quality metrics for OpenStreetMap," in *Proc. 18th SIGSPATIAL Int. Conf. Adv. Geographic Inf. Syst. Ser. (GIS '10 ACM)*, New York, NY, USA, 2010, pp. 514–517.
- [27] C. K. Robert Hecht, "Measuring completeness of building footprints in OpenStreetMap over space and time," *ISPRS Int. J. Geo-Inf.*, vol. 2, pp. 1066–1091, 2013.
- [28] A. Reigber and A. Moreira, "First demonstration of airborne SAR tomography using multibaseline L-band data," *IEEE Trans. Geosci. Remote Sens.*, vol. 38, no. 5, pp. 2142–2152, Sep. 2000.
- [29] G. Fornaro, F. Serafino, and F. Soldovieri, "Three-dimensional focusing with multipass SAR data," *IEEE Trans. Geosci. Remote Sens.*, vol. 41, no. 3, pp. 507–517, Mar. 2003.
- [30] G. Fornaro, D. Reale, and F. Serafino, "Four-dimensional SAR imaging for height estimation and monitoring of single and double scatterers," *IEEE Trans. Geosci. Remote Sens.*, vol. 47, no. 1, pp. 224–237, Jan. 2009.
- [31] X. X. Zhu and R. Bamler, "Let's do the time warp: Multicomponent nonlinear motion estimation in differential SAR tomography," *IEEE Geosci. Remote Sens. Lett.*, vol. 8, no. 4, pp. 735–739, Jul. 2011.
- [32] X. X. Zhu, "Very high resolution tomographic SAR inversion for urban infrastructure monitoring—A sparse and nonlinear tour," Ph.D. dissertation, Technische Univ. München, Munich, Germany, 2011.
- [33] K. P. Burnham and D. R. Anderson, *Model Selection and Multimodel Inference: A Practical Information-Theoretic Approach*, 2nd ed. New York, NY, USA: Springer, 2003.
- [34] D. Malioutov, M. Cetin, and A. Willsky, "A sparse signal reconstruction perspective for source localization with sensor arrays," *IEEE Trans. Signal Process.*, vol. 53, no. 8, pp. 3010–3022, Aug. 2005.
- [35] Y. Eldar and H. Rauhut, "Average case analysis of multichannel sparse recovery using convex relaxation," *IEEE Trans. Inf. Theory*, vol. 56, no. 1, pp. 505–519, Jan. 2010.
- [36] E. Aguilera, M. Nannini, and A. Reigber, "Multi-signal compressed sensing for polarimetric SAR tomography," in *Proc. IEEE Int. Geosci. Remote Sens. Symp. (IGARSS)*, Jul. 2011, pp. 1369–1372.

- [37] M. Schmitt and U. Stilla, "Compressive sensing based layover separation in airborne single-pass multi-baseline InSAR data," *IEEE Geosci. Remote Sens. Lett.*, vol. 10, no. 2, pp. 313–317, Mar. 2013.
- [38] R. Bamler, M. Eineder, N. Adam, X. Zhu, and S. Gernhardt, "Interferometric potential of high resolution spaceborne SAR," *Photogrammetrie—Fernerkundung—Geoinformation*, vol. 2009, no. 5, pp. 407–419, Nov. 2009.
- [39] N. Adam, R. Bamler, M. Eineder, and B. Kampes, "Parametric estimation and model selection based on amplitude-only data in ps-interferometry," in *Proc. ESA FRINGE Workshop*, 2005.
- [40] M. Shahzad and X. X. Zhu, "Robust reconstruction of building facades for large areas using spaceborne TomoSAR point clouds," *IEEE Trans. Geosci. Remote Sens.*, vol. 53, no. 2, pp. 752–769, Feb. 2015.



Xiao Xiang Zhu (S'10–M'12–SM'14) received the bachelor degree in space engineering from the National University of Defense Technology (NUDT), Changsha, China, in 2006. She received the Master (M.Sc.) degree, her doctor of engineering (Dr.-Ing.) degree and her "Habilitation" in the field of signal processing from Technische Universität München (TUM), Munich, Germany, in 2008, 2011, and 2013, respectively. Prof. Zhu was a Guest Scientist or Visiting Professor at the Italian National Research Council (CNR-IREA), Naples, Italy, Fudan University, Shanghai, China, and the University of Tokyo, Tokyo, Japan, in 2009, 2014, and 2015, respectively. Since 2011, she has been a Scientist with the Remote Sensing Technology Institute at the German Aerospace Center (DLR), Oberpfaffenhofen, where she is the head of the Team Signal Analysis. Since 2013, she is also a Helmholtz Young Investigator Group Leader and appointed as TUM junior fellow. In 2015, she was appointed as the Professor for Signal Processing in Earth Observation at TUM. Prof. Zhu is an associate Editor of *IEEE TRANSACTIONS ON GEOSCIENCE AND REMOTE SENSING*. Her main research interests are: advanced InSAR techniques such as high-dimensional



Nan Ge received the bachelor and the master degree in geoenvironmental engineering at TU Clausthal, Germany. He has been pursuing his doctor's degree since 2013 in the Helmholtz Young Investigators Group (SiPEO) at the Remote Sensing Technology Institute of German Aerospace Center (DLR), Germany. His work mainly involves developing advanced tomographic techniques for very high-resolution SAR systems.



Muhammad Shahzad (S'12) received the B.E. degree in electrical engineering from the National University of Sciences and Technology, Islamabad, Pakistan, and the M.Sc. degree in autonomous systems from the Bonn Rhein Sieg University of Applied Sciences, Sankt Augustin, Germany. Since December 2011, he has been working towards his Ph.D. degree at Signal Processing in Earth Observation (SiPEO), Technische Universität München (TUM), Munich, Germany. His research topic is the automatic 3-D reconstruction of objects from point clouds retrieved from spaceborne synthetic-aperture-radar image stacks.